



## Performance comparison of CO<sub>2</sub> conversion in slurry and monolith photoreactors using Pd and Rh-TiO<sub>2</sub> catalyst under ultraviolet irradiation

Oluwafunmilola Ola<sup>a</sup>, Mercedes Maroto-Valer<sup>b,\*</sup>, Dong Liu<sup>a</sup>, Sarah Mackintosh<sup>a</sup>, Chien-Wei Lee<sup>c</sup>, Jeffrey C.S. Wu<sup>c</sup>

<sup>a</sup> Centre for Innovation in Carbon Capture and Storage (CICCS), Faculty of Engineering, University of Nottingham, NG7 2RD, United Kingdom

<sup>b</sup> Centre for Innovation in Carbon Capture and Storage (CICCS), School of Engineering and Physical Sciences, Heriot-Watt University, Edinburgh, EH14 4AS, United Kingdom

<sup>c</sup> Department of Chemical Engineering, National Taiwan University, Taipei, 10617, Taiwan

### ARTICLE INFO

#### Article history:

Received 9 May 2012

Received in revised form 17 July 2012

Accepted 20 July 2012

Available online 27 July 2012

#### Keywords:

Slurry reactor

Photocatalysis

Monolith photoreactor

Titanium dioxide

### ABSTRACT

Anthropogenic activities are causing an increase in greenhouse gases in the atmosphere, with carbon dioxide (CO<sub>2</sub>) being the key cause of global warming. The conversion of CO<sub>2</sub> into valuable hydrocarbons serves as a promising route for mitigating the effects of global warming and meeting future energy demands. Herein, we show the comparison between the photocatalytic reduction of CO<sub>2</sub> for metal coated TiO<sub>2</sub> nanoparticles in a slurry batch annular reactor system and metal coated TiO<sub>2</sub> monoliths in an internally illuminated photoreactor system using the 1 wt% Pd/0.01 wt% Rh-TiO<sub>2</sub> catalyst. Carbon based fuels, such as methane, methanol or acetaldehyde were produced in the gas phase from the CO<sub>2</sub> reduction with water by titania nanoparticles modified by Pd and Rh for improved reactivity. The modified photocatalysts synthesized by the improved sol-gel method were tested under UV light irradiation. The quantum efficiency of the internally illuminated monolith reactor was near one order of magnitude higher than the slurry batch annular reactor. This efficiency was due to the reactor's flexible configuration; which allows maximum exploitation of the combined advantages of the high surface area of the monolith and the elimination of uneven light distribution via the optical fibres.

© 2012 Elsevier B.V. All rights reserved.

## 1. Introduction

Until a non-carbon fuel source can be successfully developed to meet global demands, solar fuel production serves an important strategy for meeting future energy demands and mitigating the effects of global warming. Carbon based fuels can be produced from the conversion of carbon dioxide (CO<sub>2</sub>) by photocatalysts capable of simultaneously driving chemical reactions and utilising solar energy [1]. Amongst these photocatalysts, titanium dioxide (TiO<sub>2</sub>) still remains the most researched semiconductor material due to its widespread applications [2]. For photocatalysis, of utmost importance is the ability of TiO<sub>2</sub> to harness solar energy, be chemically stable and nontoxic [2]. However, since it exhibits low photocatalytic activity for CO<sub>2</sub> reduction; research has focused on ways of improving the functional properties and photocatalytic activity of TiO<sub>2</sub> based materials. Modification of the optical and electronic properties of TiO<sub>2</sub> serves as one of such routes and can be achieved by doping with metals such as Cu [3,4], Pd [5] and Rh [6]. When these metals are incorporated into the interstitial sites, replaced

with Ti in the substitutional sites or aggregated on the surface of TiO<sub>2</sub>, they can cause changes in the properties of TiO<sub>2</sub> [7]. The band structures and properties of TiO<sub>2</sub> have been reported to be tailored by this process. These metals also serve as a source of charge-carrier traps which can increase the life span of separated electron hole pairs, and thus enhancing the efficiency and product selectivity for CO<sub>2</sub> photoreduction [8].

The configuration of catalyst particles in a photoreactor system is also another factor that can influence the overall photocatalytic efficiency [9,10]. Catalysts can either be suspended in aqueous solutions or immobilized onto supports. When powders are suspended in liquid medium; the quantum efficiency of the catalyst, absorption properties of both reactants and non-reactants in solution and surface light intensity determines the rate of reaction [10]. Some of the key advantages of this system are that there is entire external surface illumination during reaction time if the particle size of the catalyst is small; with phase segregation not occurring if the solution is homogeneously mixed [9]. However, the penetration depth of UV light into the reaction medium can be limited by the strong light absorption of organic species and catalyst particles [10]. A large proportion of catalyst surface area might be inactive due to low photon energy received, as most of the light irradiation is lost due to absorption by liquid when light approaches the catalyst through the bulk liquid phase [11,12].

\* Corresponding author at: Department of Chemical Engineering, Heriot-Watt University, Edinburgh, United Kingdom. Tel.: +44 131 451 8028.

E-mail address: [m.maroto-valer@hw.ac.uk](mailto:m.maroto-valer@hw.ac.uk) (M. Maroto-Valer).

The textural properties such as specific surface area and porosity of the immobilized catalysts can be enhanced by immobilising them onto supports [9]. However, the photocatalyst must be strongly adhered to the support and have light absorption properties to be effective. There must also be strong surface chemical–physical bonding between the photocatalyst and the support; which must not negatively affect the activity of the photocatalyst [13]. Mass transfer limitations and low light utilization efficiency due to little or no light absorption in the pores or channels of the catalyst coated supports are also key limitations [14].

In order to reduce these limitations associated with catalyst supports for CO<sub>2</sub> photoreduction, previous researchers [15–17] have designed photoreactors using supports such as optical fibres and monoliths. The conventional optical fibre reactor (OFR) has been modified by using fibres with different cores and coatings [18,19], increasing their diameter to create ease of handling and the use of cooling systems [20] to eliminate the limitation of heat build-up. In particular, previous CO<sub>2</sub> photoreduction studies conducted by Nguyen and Wu [21] using optical fibres coated with Cu–Fe/TiO<sub>2</sub> catalysts in the gaseous phase have demonstrated that the number of optical fibres can determine the rate of ethylene production and selectively increase or decrease the quantum yield. A maximum yield of 0.91 μmol/g-cath was observed using the loading ratio of 0.5 wt% Cu–Fe/TiO<sub>2</sub> for methane production.

Lin and Valsaraj [22] described the use of monolith as a catalyst immobilization medium presenting higher surface area compared to beads and plates. They further improved the configuration of the monolith reactor by using coated optical fibres placed in the channels of the monolith substrate. Du et al. [23] and Carneiro et al. [18] changed this arrangement by coating the inner surface of the monolith with catalysts instead of the fibres. They reported that monolith coating provided maximum exploitation of the combined advantages of the monolith and conventional optical fibre reactor system by eliminating heat build-up which could lead to the rapid deactivation of the catalyst coated fibres as a result of direct contact and uneven light and catalyst distribution due to fibre abrasion [20].

More recently, further enhancement to this arrangement has been demonstrated by incorporating different designs of polymethylmethacrylate (PMMA) optical fibres into the catalyst coated monolith [24]. In this case, the PMMA fibres with tip-reflection and mid-carves were found to be able to transmit light to effectively illuminate the channels of the NiO–InTaO<sub>4</sub> coated monolith and increase yield. Although previous studies have focused on the modification of titania with Pd and Rh [5,6]; the combined role of these metals loading on the performance of TiO<sub>2</sub> for CO<sub>2</sub> reduction has not been studied, neither has their effect on supports such as the monolith been explored. Accordingly, this study aims to immobilise metal loaded TiO<sub>2</sub> onto ceramic honeycomb monolithic structures threaded with optical fibres to increase contact efficiency, active sites and eliminate limited light penetration through the internal channels. The results from this catalyst configuration are also compared to suspended TiO<sub>2</sub> nanoparticles in H<sub>2</sub>O. Detailed characterizations to understand the influence of key process parameters on these samples were investigated.

## 2. Experimental

### 2.1. Preparation of metal loaded TiO<sub>2</sub> nanoparticles

Metal loaded TiO<sub>2</sub> nanoparticles were synthesized by the improved sol–gel method [25]. In a typical synthesis procedure, 6.8 ml of titanium (IV) butoxide (99% Acros Organics) was added to 5.92 ml of n-butanol (Fisher Scientific) under stirring. The desired amount of metal precursor(s), i.e. palladium (II) nitrate hydrate (Pd (NO<sub>3</sub>)<sub>2</sub>·2H<sub>2</sub>O, Acros Organics), rhodium (II) acetate (Rh<sub>2</sub>(CH<sub>3</sub>CO<sub>2</sub>)<sub>4</sub>,

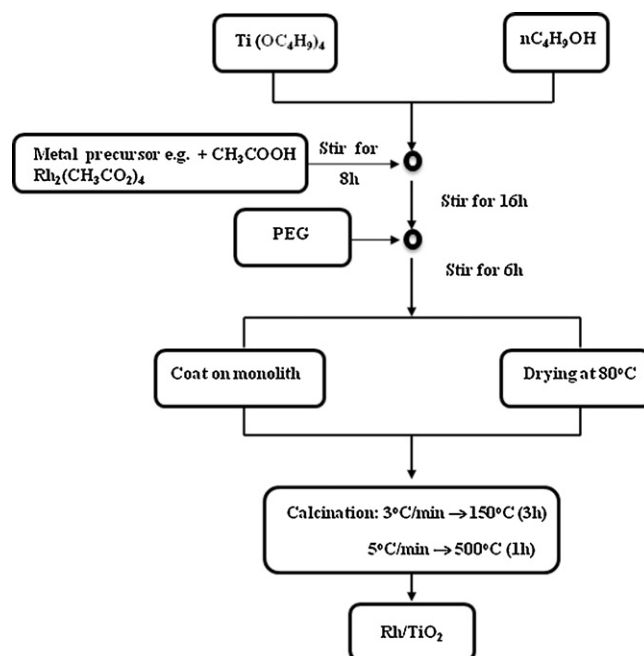


**Fig. 1.** Metal loaded sol procedure.

Sigma Aldrich) was suspended in 4.8 ml of acetic acid (99.8% Acros Organics). The two solutions were magnetically stirred together at room temperature for 6 h to allow esterification reactions occur. The homogeneous mixture was then dried in a chamber furnace (Carbolite, CWF 1100) at 150 °C for 2 h and calcined at 500 °C for 1 h to burn off organic compounds and complete crystallization. The resulting sample was crushed into fine powder to obtain metal loaded TiO<sub>2</sub> nanoparticles. To investigate the effect of loading different amounts of Pd and Rh on the photocatalytic performance on TiO<sub>2</sub> nanoparticles, single and co-doped TiO<sub>2</sub> nanoparticles with different amount of Pd and Rh (0.01–1.5 wt%) were loaded simultaneously under identical experimental conditions. Amongst the single loaded catalysts, 1 wt% Pd and 0.01 wt% Rh gave the maximum performance, and therefore, these ratios were then used for co-doping.

### 2.2. Preparation of metal coated TiO<sub>2</sub> monoliths

The 177 channels per 2 mm × 2 mm aperture honeycomb monoliths with dimensions of 4 cm (diameter) by 5 cm (length) were supplied by Chauger Honeycomb Ceramics Company, Taiwan. Monoliths were cleaned by ultrasonification in deionised water for 40 min and dried at 80 °C for 48 h. After drying, the monoliths were pre-coated with silica (SiO<sub>2</sub>) sol before metal loading by the method reported by Liou et al. [24]. This was done to ensure catalyst deposition on top of the SiO<sub>2</sub> layer, where it could be photocatalytically active instead of being buried within the pores.

The pre-coated SiO<sub>2</sub> monoliths were coated with metal loaded TiO<sub>2</sub> sol following the procedure shown in Fig. 1. Titanium (IV) butoxide was added to n-butanol with a volume ratio of 1:4 (Titanium (IV) butoxide: n-butanol). A known amount of 1 wt% Pd (NO<sub>3</sub>)<sub>2</sub>·2H<sub>2</sub>O and 0.01 wt% Rh<sub>2</sub>(CH<sub>3</sub>CO<sub>2</sub>)<sub>4</sub> were added singly and jointly to acetic acid. The two solutions were stirred together for 16 h. Subsequently, polyethylene glycol (PEG) solution was added to the metal loaded sol to prevent cracking of the coated layers during drying and enhance viscosity. After 6 h, the pre-coated SiO<sub>2</sub> monolith was then dip-coated with this sol. The excess solution was blown from the channels of the monolith using an air-jet gun. The coated monolith was then dried by heating from ambient

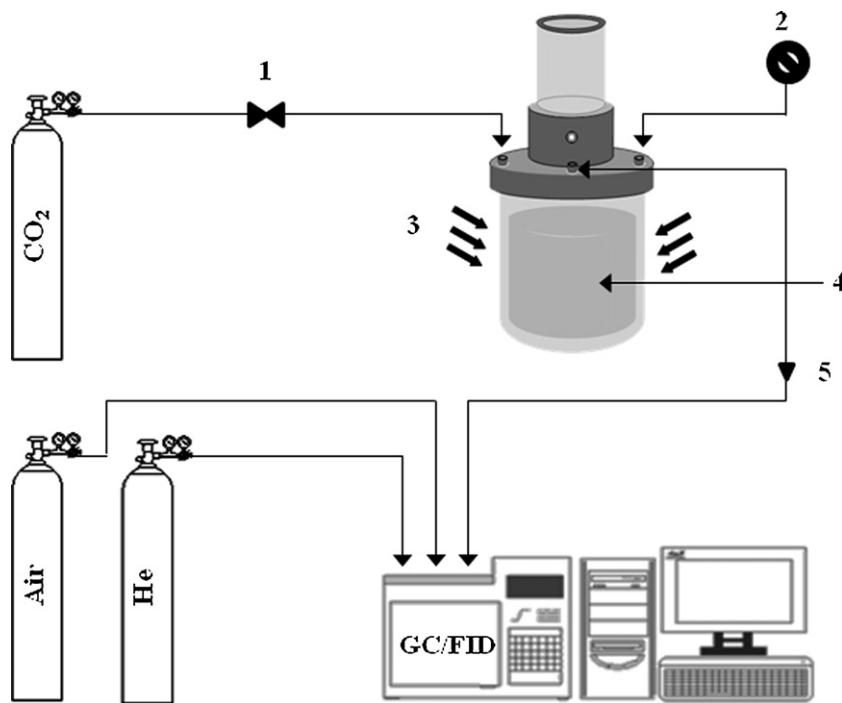


**Fig. 2.** Schematics of the stirred batch annular photoreactor: (1) switch valve; (2) pressure gauge; (3) UV light source; (4) suspended catalyst in H<sub>2</sub>O; (5) CO<sub>2</sub> + products.

temperature at 3 °C/min to 150 °C for 3 h. Calcination was done at 5 °C/min to 500 °C for 1 h.

### 2.3. Characterization

The morphology and elemental composition of the prepared samples were characterized by scanning electron microscopy-energy dispersive spectroscopy (SEM-EDS, Quanta 600 model). Powder X-ray diffraction patterns were obtained using a Hilton-brooks X-ray powder diffractometer. Scherrer's equation was used for estimating the crystallite size. Nitrogen adsorption/desorption isotherms at 77 K as a function of relative pressure were obtained by a Micromeritics ASAP V3.01 G 2020 instrument using a static volumetric technique. The band gap, threshold wavelength and the absorbance of ultraviolet light as a function of the transmittance were measured using the diffusive reflective ultraviolet-visible spectrophotometer (Varian Cary 300). Approximately 2 g of powder samples were loaded in a quartz cell with the spectral range between 200–800 nm recorded. Changes in the porosity of the monoliths were characterized using the mercury porosimetry analyser (Micromeritics Autopore IV 9500 V1.05). Approximately 0.3–0.4 g of samples were loaded in the penetrometer and scanned within the range of 0.1–60,000 psia. X-ray photoelectron spectroscopy (XPS) was performed by using a Kratos AXIS ULTRA with a mono-chromated Al K $\alpha$  X-ray source (1486.6 eV) typically operated at 3 mA emission current and 12 kV anode potential. The high resolution scans were charge corrected to the main C 1s peak = 285 eV and then quantified to compare the amounts of each element present, using CASAXPS software with Kratos sensitivity factors.

### 2.4. CO<sub>2</sub> photocatalytic reduction

#### 2.4.1. Stirred batch annular photoreactor

CO<sub>2</sub> photoreduction was evaluated in aqueous solution using a stirred batch annular photoreactor of dimensions of 8.9 cm × 7.9 cm (diameter and height) with ports for sampling the aqueous and gaseous products, measuring the pressure and gas (CO<sub>2</sub>) inlet

(Fig. 2). The photoreactor was irradiated from both sides of the quartz vessel using two 8 W UVA lamps each (Sylvania) with dimensions of 16 mm and 150 mm (diameter and height). The wavelength of UV radiation inside the reactor was 365 nm with average light intensity of 3.22 mW/cm<sup>2</sup>. The reactor was enclosed inside a gloved box to exclude any external light source, prevent UV leakage and maximise light energy within the reactor. The light intensity was determined by a UVA digital radiometer that was placed inside the reactor prior to the experiment. Catalyst powder (1 g) suspended in 200 ml of deionised water was magnetically stirred at 240 rpm to ensure continuous mixing and thus preventing sedimentation. Ultra pure CO<sub>2</sub> (Air Products, 99.999%) gas was bubbled through the assembled photoreactor at 1 bar for 20 min to saturate the solution and eliminate air completely. The solution was further pressurized at 1 bar for another 15 min, and then the CO<sub>2</sub> supply was cut off. The UV lamps were switched on and the curtains of the gloved box shut for 1.5 h to enable photoreduction take place. Aliquots of liquid and gas samples were injected into the gas chromatograph (Thermo-Fisher, trace GC) equipped with flame ionisation detector (FID) using the RT-Alumina capillary column for identifying and analysing the extracted samples, specifically for methane. Blank reactions were performed with and without the light source in the presence and absence of the catalyst to confirm that reactions were due to CO<sub>2</sub> photoreduction. Methane was found to be the major product in the gas phase, with other products such as acetaldehyde and methanol not being observed within the detection limit of the GC for hydrocarbons, 0.05 µg/ml in both the liquid and gas phase.

#### 2.4.2. Internally illuminated monolith photoreactor

Gas-phase photoreduction studies were carried out using the internally illuminated monolith photoreactor shown in Fig. 3. The optical fibres (Shiner Fibre Optics, Taiwan) were uniformly distributed in the monolith and placed into a cylindrical Pyrex glass reactor with dimensions of 5.5 cm × 11 cm (diameter and height). Light was irradiated into the reactor through the quartz window by the high pressure mercury lamp (Exfo Omnicure S1500). The light wavelength was adjusted using 320–500 nm filters to obtain

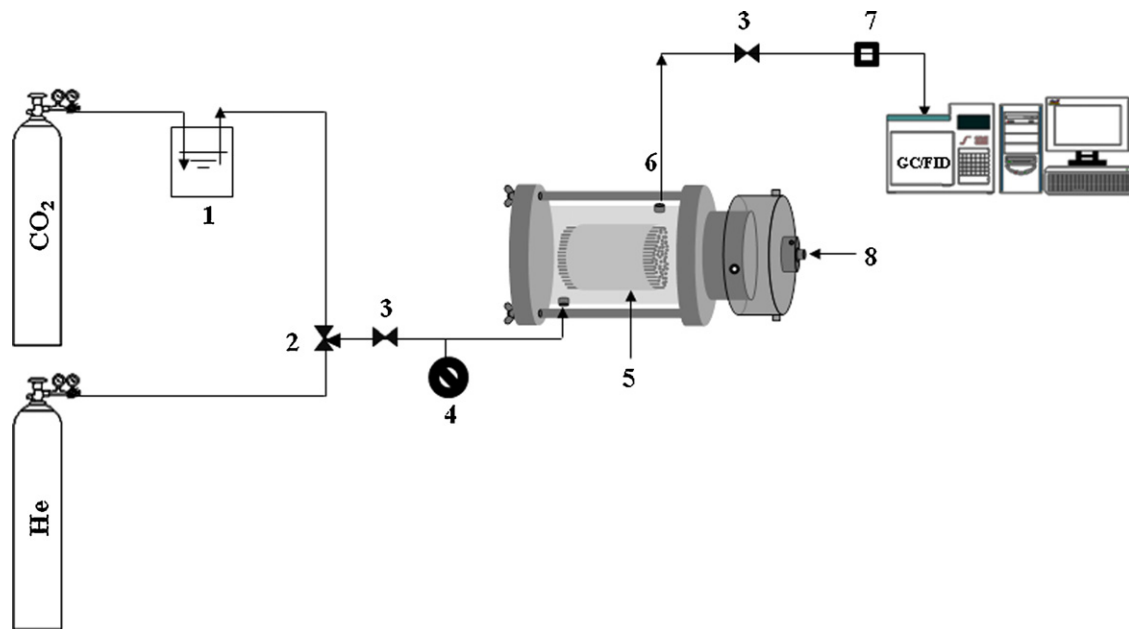


**Fig. 3.** Schematics of the internally illuminated monolith photoreactor: (1) water saturator; (2) 3-way valve; (3) 2-way valve; (4) pressure gauge; (5) monolith with optical fibres; (6) gas outlet tube; (7) flow meter; (8) UV light guide.

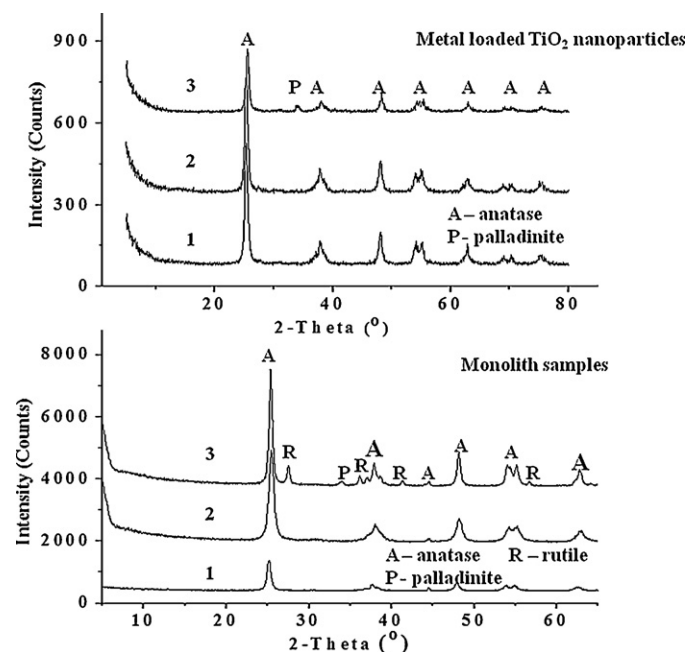
average optimal light intensity of  $41.62 \text{ mW/cm}^2$  (measured in front of the quartz window). The reactor was wrapped in aluminium foil and placed in the gloved box to avoid external light interference. Leakage was tested by observing changes in the pressure gauge when purging with Helium (He) gas. If leak-proof, the reactor was then purged with He for 1 h, then switched to  $\text{CO}_2$  gas saturated with water vapour for 1 h at flow rate of 4 ml/min. The retention time (volume/flow rate) of the monolith was 54 min. After 1 h, the light source was turned on and light intensity readings were taken at hourly intervals. The flow of  $\text{CO}_2$  saturated with water vapour was continuous throughout the reaction. Products were analyzed using a gas chromatograph (China Chromatograph, Taiwan) equipped with FID using a Porapak QS column. Blank reactions were performed and no hydrocarbons were detected.

### 3. Results and discussion

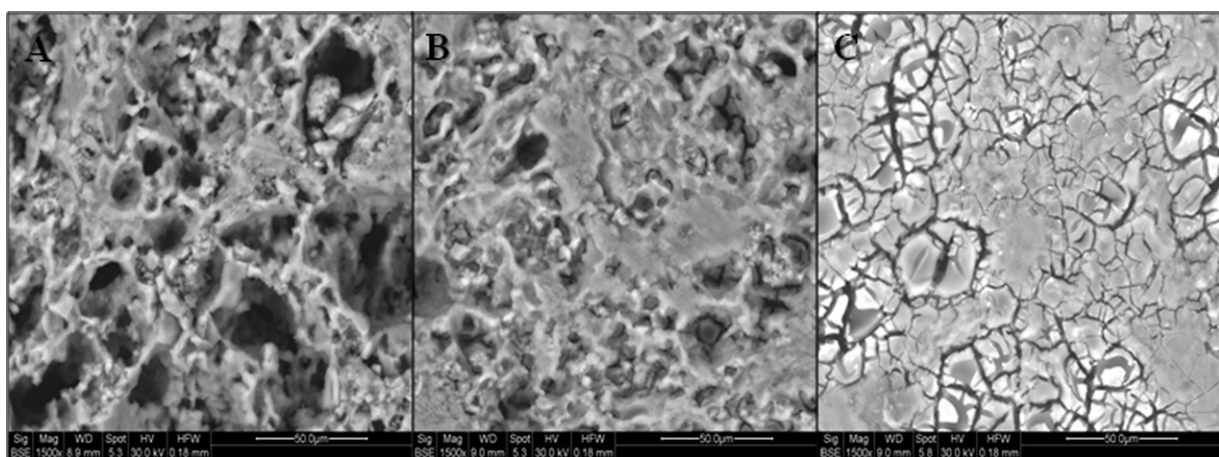
#### 3.1. Morphology and phase structures

Fig. 4 shows the XRD patterns of  $\text{TiO}_2$ , 0.01 wt% Rh- $\text{TiO}_2$  and 1 wt% Pd/0.01 wt% Rh- $\text{TiO}_2$  for the metal loaded nanoparticles and monolith samples. After calcination at  $500^\circ\text{C}$ , all diffraction peaks for the metal loaded nanoparticles can be indexed to the tetragonal anatase phase  $\text{TiO}_2$  which was confirmed by comparison with the Joint Committee on Powder Diffraction Standards (JCPDS) Card File no. 21-1272. The phase structures of Pd elements on the surface of  $\text{TiO}_2$  nanoparticles were observed by the characteristic diffraction peaks of palladinite ( $\text{PdO}$ ) at ca.  $33.8^\circ$  (JCPDS Card File no. 41-1107) for the 1 wt% Pd/0.01 wt% Rh- $\text{TiO}_2$  sample of both metal loaded nanoparticles and monoliths. Addition peaks of palladium (Pd) at ca.  $40.1^\circ$  and  $46.6^\circ$  (JCPDS Card File no. 46-1043) were further observed in the 1 wt% Pd/0.01 wt% Rh- $\text{TiO}_2$  sample of the metal loaded nanoparticles only. No diffraction peak of Rh was observed in both metal loaded nanoparticles and monolith samples due to low metal loading ratio. The diffraction patterns suggest that the samples are well crystallized and these metals can be successfully coated on the surface of  $\text{TiO}_2$  nanoparticles with the crystallite grain size for anatase within 10.10–14.92 nm (Table 1). Additional peaks of rutile were detected for monolith samples of  $\text{TiO}_2$  and 1 wt%

Pd/0.01 wt% Rh- $\text{TiO}_2$  at ca.  $27.44^\circ$ ,  $36.08^\circ$  and other positions. The peak of rutile was not detected in the 0.01 wt% Rh- $\text{TiO}_2$  sample by XRD as the ionic radius of  $\text{Rh}^{3+}$  is the same as that of  $\text{Ti}^{4+}$ , i.e.  $0.68 \text{ \AA}$ , Rh ions can be easily incorporated into the crystal lattice of  $\text{TiO}_2$  [26]. This could also be due to the low metal content and the high dispersion of Rh all through the structure of  $\text{TiO}_2$ . Conversely, the 1 wt% Pd/0.01 wt% Rh- $\text{TiO}_2$  sample indicates an increased growth of rutile nuclei due to the 1% metal loading of palladium creating a number of defects within the anatase phase. This is in agreement with other methods where different loading ratios were used [7]. The relative intensity of the main anatase peak (101) of the monolith samples was higher than the metal loaded nanoparticles,



**Fig. 4.** XRD patterns of (1)  $\text{TiO}_2$  (2) 0.01 wt% Rh- $\text{TiO}_2$  (3) 1 wt% Pd/0.01 wt% Rh- $\text{TiO}_2$  for (left) metal loaded nanoparticles and (right) monolith samples.



**Fig. 5.** SEM micrographs of (A) Bare monolith (B)  $\text{SiO}_2$  coated monolith (C) 1 wt% Pd/0.01% Rh-TiO<sub>2</sub> on  $\text{SiO}_2$  monolith samples.

**Table 1**

		Crystallite size (anatase, nm)	Surface area (m <sup>2</sup> /g)	Bandgap (eV)
Metal loaded nanoparticles	TiO <sub>2</sub>	13.83	40.69	3.08
	0.01 wt%	13.85	46.44	2.98
	Rh-TiO <sub>2</sub>			
	1 wt%	14.42	47.47	2.96
	Pd/0.01 wt%			
	Rh-TiO <sub>2</sub>			
	TiO <sub>2</sub>	14.92	26.72	3.10
	0.01 wt%	12.52	43.44	2.95
	Rh-TiO <sub>2</sub>			
	1 wt%	10.57	51.13	2.91
Monolith samples	Pd/0.01 wt%			
	Rh-TiO <sub>2</sub>			

with peak broadening occurring due to the decrease in crystallite size. The crystallite grain size for rutile was 12.04 nm for TiO<sub>2</sub> and 23.12 nm for 1 wt% Pd/0.01 wt% Rh-TiO<sub>2</sub>, respectively. The specific surface area of both the metal loaded nanoparticles and monoliths are shown in **Table 1**. An increase in specific surface area occurs as TiO<sub>2</sub> is loaded with metals for the metal loaded nanoparticles and monolith samples.

Aggregates of irregular shaped particles of homogeneous shapes and varying sizes in the range of 40–110 nm were observed from the SEM micrographs of 0.01 wt% Rh and 1 wt% Pd/0.01 wt% Rh catalyst using the magnification of 20,000×. No significant difference in morphology could be seen from the micrographs of the metal loaded TiO<sub>2</sub> nanoparticles compared to pure TiO<sub>2</sub>. The morphology of the pores of the bare monolith and the SiO<sub>2</sub> pre-coated monolith are illustrated in **Fig. 5a** and b, respectively. The catalysts were uniformly dispersed on the surface of the pre-coated SiO<sub>2</sub> layer (**Fig. 5c**) instead of being embedded within the pores of the monolith. To further investigate the effect of coating SiO<sub>2</sub> on the bare monolith, changes in porosity before and after SiO<sub>2</sub> coating were characterized by mercury porosimetry. **Table 2** shows the decrease

in porosity of the monolith from 20.39% to 9.53% after two layers of SiO<sub>2</sub> coating. This is in good agreement with the SEM results of the monoliths which indicate that the pores were filled with SiO<sub>2</sub>.

### 3.2. XPS analysis

The XPS spectra of Rh 3d and Pd 3d on 1 wt% Pd/0.01 wt% Rh-TiO<sub>2</sub> for both the powder and monolith samples are presented in **Fig. 6**. Two broad peaks observed for the 1 wt% Pd/0.01 wt% Rh-TiO<sub>2</sub> in both samples can be indexed to the Pd 3d spin orbit splitting into 3d<sub>3/2</sub> and 3d<sub>5/2</sub>. For the metal loaded nanoparticles, the Pd 3d<sub>3/2</sub> peaks formed a doublet with signals occurring at 341.6 eV and 342.2 eV. The peak at 341.6 eV corresponds to base palladium metal, while the other at 342.2 eV corresponds to the oxide present in Pd [27,28]. The signal at 336.4 eV for Pd 3d<sub>5/2</sub> is attributable to PdO<sub>x</sub>/Pd. For the monolith samples, the peaks at 336.6 eV and 341.8 eV correspond to both the oxide present in Pd and metallic Pd [27,28]. Two broad peaks for Rh observed in both samples can be indexed to the Rh 3d spin orbit splitting into 3d<sub>3/2</sub> and 3d<sub>5/2</sub>. The 3d<sub>3/2</sub> peaks for both metal loaded nanoparticles and monolith samples appear at identical positions of 309.6 eV which corresponds to Rh<sub>2</sub>O<sub>3</sub> [27]. The Rh 3d<sub>5/2</sub> peaks for the monolith sample appears at 314.4 eV, while the peaks appear at 313.6 eV and 314.5 eV, respectively, for the metal loaded nanoparticles.

### 3.3. UV-vis analysis

The effect of Pd and Rh loading on TiO<sub>2</sub> nanoparticles was observed by the UV-vis spectra, as shown in **Fig. 7**. The band gap energies were in the range of 2.91–3.10 eV. The band gap absorption of TiO<sub>2</sub> for both the metal loaded nanoparticles and monolith samples exhibited similar absorption edges of ca. 400 nm. The band gap energies of the catalysts decreased upon the addition of Pd and Rh, causing a slight shift towards the visible light region. Aside from the slight decrease in band gap energy observed for all the catalysts compared to TiO<sub>2</sub>, the shift towards visible light could be due to the defect centres created from the substitution of Ti<sup>4+</sup> by Pd<sup>2+</sup> and Rh<sup>3+</sup> atoms in the crystal lattice [7]. For the co-doped Pd samples, the presence of Pd and Rh also decreased the band gap energy when compared to the band gap energy of pure TiO<sub>2</sub>. The results are comparable to reported studies on metal loaded TiO<sub>2</sub> catalyst [14].

**Table 2**

Mercury porosimetry of bare and metal loaded TiO<sub>2</sub> monoliths.

	Bare monolith	SiO <sub>2</sub> -monolith	TiO <sub>2</sub> /SiO <sub>2</sub> -monolith
Porosity (%)	20.39	9.53	3.76
Total intrusion volume (ml/g)	0.20	0.15	0.12

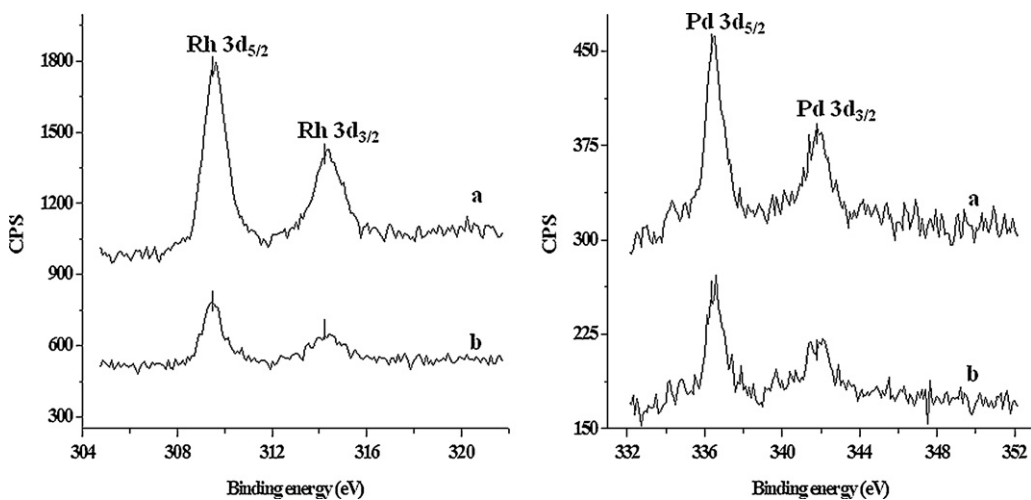


**Fig. 6.** XPS spectra of Rh3d and Pd3d of 1 wt% Pd/0.01% Rh-TiO<sub>2</sub> catalyst (monolith (A) and powder (B) samples).

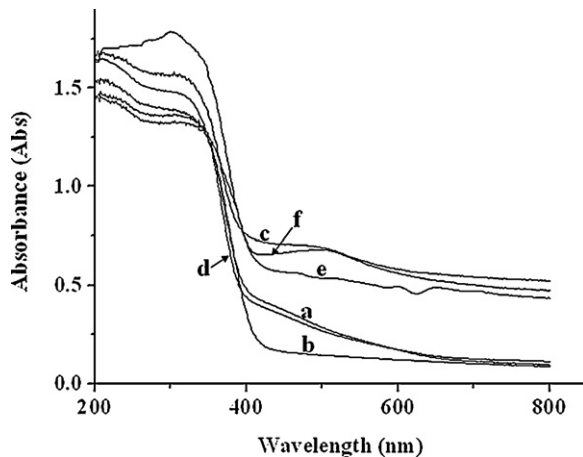


**Fig. 7.** UV-vis spectroscopy of powder (A) TiO<sub>2</sub> (B) 0.01 wt% Rh-TiO<sub>2</sub> (C) 1 wt% Pd/0.01 wt% Rh-TiO<sub>2</sub> and monolith (D) TiO<sub>2</sub> (E) 0.01 wt% Rh-TiO<sub>2</sub> (F) 1 wt% Pd/0.01 wt% Rh-TiO<sub>2</sub> samples.

### 3.4. Photoreduction of CO<sub>2</sub> with H<sub>2</sub>O

#### 3.4.1. Slurry batch annular reactor system

Table 3 shows the production rate of methane over various metal loaded TiO<sub>2</sub> nanoparticles under UVA. Methanol and acetaldehyde were not detected within the detection limit of the GC for hydrocarbons which is 0.05 µg/ml. The experiments were repeated thrice for verifying the reproducibility and the error was determined to be within the range of ±0.02 to ±0.07. It was observed that the loading of TiO<sub>2</sub> with Pd and Rh enhanced the photocatalytic conversion compared to pure TiO<sub>2</sub>. The optimum amount of Pd and Rh loading on TiO<sub>2</sub> was found to be 1 wt% and 0.01 wt% for the single Pd and Rh loaded catalyst, respectively. Amongst these catalysts, the maximum production of methane,

0.06 µmol/g-cat h and 0.04 µmol/g-cat h was observed over the 1 wt% Pd-TiO<sub>2</sub> and 0.01 wt% Rh-TiO<sub>2</sub> catalyst, respectively, using the stirred batch annular photoreactor following 1.5 h of light irradiation (Table 3). After the optimal loading ratio of 1 wt%, a decrease in photocatalytic activity was observed using higher loading ratios. Therefore, the loading ratio of 1 wt% Pd was chosen for co-doping with Rh to determine if the photocatalytic activity could be further improved. Using the co-doped catalyst, 1 wt% Pd/0.01 wt% Rh-TiO<sub>2</sub>, methane production decreased to 0.03 µmol/g-cat h, while it increased to 0.07 µmol/g-cat h using the 1 wt% Pd/0.006 wt% Rh-TiO<sub>2</sub> after 1.5 h of light irradiation. This result could be due to the coverage of the surface of TiO<sub>2</sub> from the increased metal concentration and thus inhibiting interfacial charge transfer due to insufficient amount of light energy available for activation of all the catalyst particles. Tseng et al. [29] reported that the high concentration of metal particles, i.e. >2 wt% Cu can reduce photon absorption by TiO<sub>2</sub>, and thus resulting in lower efficiency. The mixing speed and the light source arrangement (placed at opposite sides of the reactor) can also be contributing factors, as the exposure of the catalyst to light irradiation and contact efficiency between the catalyst and reactants will be determined by these factors [12]. Although the concentration of methanol and acetaldehyde were negligible in the liquid and gas phase, this result is consistent with literature which indicates that methane is the major product for CO<sub>2</sub> photoreduction using Pd deposited TiO<sub>2</sub> in the slurry reactor [30,31]. The production rate of methane was found to be 35 times higher than pure TiO<sub>2</sub>, with little or no methanol and acetaldehyde production observed in their system. These hydrocarbons were also not detected in the liquid phase when we carried out parallel experiments in our slurry photoreactor system using copper as a support system [4].

#### 3.4.2. Internally illuminated monolith reactor system

Table 4 presents the production rate of methanol and acetaldehyde over different kinds of catalyst when the monolith was used as a catalyst support. The experiments were repeated thrice to check for reproducibility and the error was within the range of ±0.01 to ±0.10. Acetaldehyde and methanol were found to be the major products in the gas phase, with the concentration of other products such as methane not detected within the detection limit of the GC for hydrocarbons which is 0.05 µg/ml. TiO<sub>2</sub> shows negligible activity compared to the metal coated monolithic catalyst. When the 1 wt% Pd was loaded on TiO<sub>2</sub>, only acetaldehyde production was observed, while methanol and acetaldehyde production were observed using the 0.01 wt% Rh catalyst. Conversely, when Pd

**Table 3**

Methane production rate over metal loaded TiO<sub>2</sub> nanoparticles under UVA.

Photocatalyst	Methane production rate (µmol/g-cat h) <sup>a</sup>
TiO <sub>2</sub>	Trace
0.01 wt% Rh-TiO <sub>2</sub>	0.04 ± 0.04
1 wt% Pd-TiO <sub>2</sub>	0.06 ± 0.10
1 wt% Pd/0.006 wt% Rh-TiO <sub>2</sub>	0.07 ± 0.06
1 wt% Pd/0.01 wt% Rh-TiO <sub>2</sub>	0.03 ± 0.02

<sup>a</sup> Production rate was derived following 1.5 h of light irradiation.

**Table 4**

Methanol and acetaldehyde production rate over metal loaded TiO<sub>2</sub> monoliths under UVA irradiation.

Photocatalyst	Methanol production rate ( $\mu\text{mol/g-cat h}$ ) <sup>a</sup>	Acetaldehyde production rate ( $\mu\text{mol/g-cat h}$ ) <sup>a</sup>
TiO <sub>2</sub>	Trace	Trace
0.01 wt% Rh-TiO <sub>2</sub>	0.06 ± 0.02	0.04 ± 0.01
1 wt% Pd-TiO <sub>2</sub>	0.00	0.06 ± 0.10
1 wt% Pd/0.006 wt% Rh-TiO <sub>2</sub>	0.02 ± 0.07	0.03 ± 0.05
1 wt% Pd/0.01 wt% Rh-TiO <sub>2</sub>	0.10 ± 0.10	0.21 ± 0.10

<sup>a</sup> Production rate was derived from the average production rate following 4 h of light irradiation.

and Rh were employed as co-dopants, decreased product formation was observed with the using the 1 wt% Pd/0.006 wt% Rh-TiO<sub>2</sub> catalyst. Conversely, improved average acetaldehyde production rate of 0.21  $\mu\text{mol/g-cat h}$  was measured using the 1 wt% Pd/0.01 wt% Rh-TiO<sub>2</sub> catalyst after 4 h.

Parallel phenomenon was demonstrated when Rh was deposited on pure TiO<sub>2</sub> and WO<sub>3</sub>-TiO<sub>2</sub> [6]. The deposition of Rh on pure TiO<sub>2</sub> and WO<sub>3</sub>-TiO<sub>2</sub> was found to influence product selectivity and production, as methanol and formic acid production were only observed on these catalysts and not on WO<sub>3</sub>-TiO<sub>2</sub> [6]. The electronic interaction between Rh and TiO<sub>2</sub> is attributed to their different work functions (4.98 eV for Rh and 4.6 eV for TiO<sub>2</sub>) [6,32]. Since the work function of the electrons in Rh and Pd (varies from 5.0 to 5.12 eV) [33,35] is larger than that of the semiconductor, TiO<sub>2</sub>, electrons will flow from the semiconductor to these metals [6,33]. Electron donating activities on Rh and Pd surfaces may promote CO<sub>2</sub> activation to form the radical anion, CO<sub>2</sub><sup>−</sup>. Light irradiation of the adsorbed layer containing CO<sub>2</sub> can enhance the extent of electron transfer with its surface concentration of the adsorbate further increasing and undergoing CO<sub>2</sub> reduction [34]. The production of hydrocarbons can thus be ascribed to the transfer of electrons from TiO<sub>2</sub> to Rh and/or Pd which participated in CO<sub>2</sub> reduction before electron-hole recombination or oxidation reaction occurred on the surface of TiO<sub>2</sub>.

Fig. 8 shows the effect of reaction time on the production rate of methanol and acetaldehyde using the 0.01 wt% Rh-TiO<sub>2</sub> catalyst. The rate of methanol production steadily increases to ca. 0.14  $\mu\text{mol/g-cat h}$  till the 11th hour when the experiment was stopped. Conversely, acetaldehyde production steadily increased to ca. 0.12  $\mu\text{mol/g-cat h}$  in 9 h. This phenomenon could be due to some of the methanol generated being oxidized to acetaldehyde. Subsequently, the decrease was due to the oxygen evolved being used

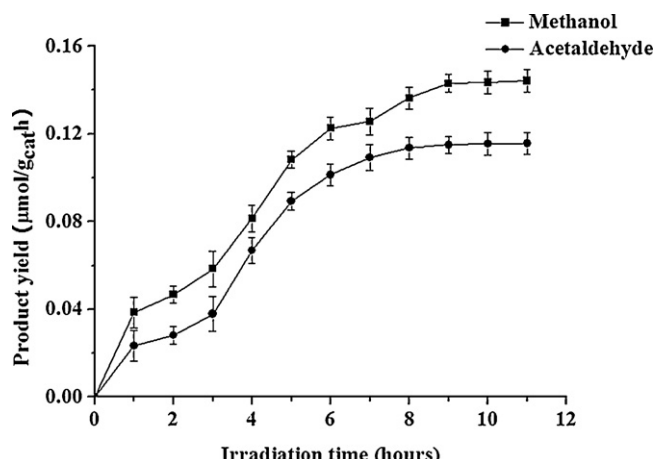


Fig. 8. The effect of reaction time on product rate using the 0.01% Rh-TiO<sub>2</sub> monolith sample.

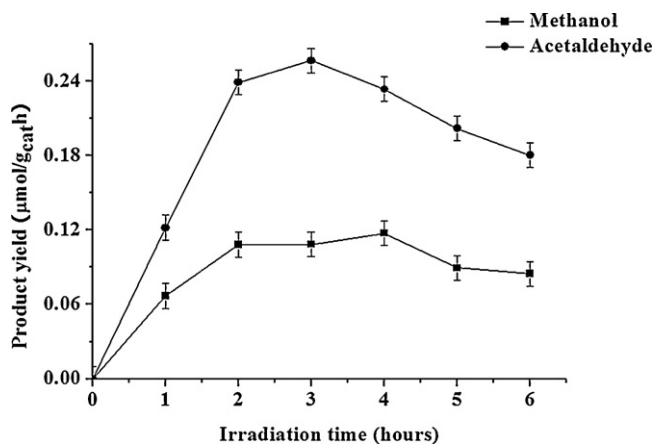


Fig. 9. The effect of reaction time on product rate using the 1 wt% Pd/0.01% Rh-TiO<sub>2</sub> monolith sample.

up for methanol generation since this reaction requires 6 photoelectrons as opposed to 12 photoelectrons needed for acetaldehyde formation. Fig. 9 shows the effect of reaction time on the production rate of methanol and acetaldehyde using the 1 wt% Pd/0.01 wt% Rh-TiO<sub>2</sub> catalyst. Acetaldehyde formation on this catalyst was more favourable compared to methanol formation. Maximum acetaldehyde formation rate of ca. 0.26  $\mu\text{mol/g-cat h}$  was achieved after 3 h, while the rate of ca. 0.12  $\mu\text{mol/g-cat h}$  was attained for methanol production after 4 h. There was a decline in product formation rate for this catalyst after these hours which were probably due to re-oxidation of methanol and insufficient photon energy to drive the reaction. Catalyst deactivation was probably due to some coverage of reaction intermediates on active sites [36].

Overall, the presence of metals enhanced the photo-activity of TiO<sub>2</sub>, with the metal loaded TiO<sub>2</sub> coated monoliths demonstrating better product formation rates than the metal loaded TiO<sub>2</sub> nanoparticles suspended in the slurry reactor. This was probably due to increased light utilization efficiency and better contact efficiency between the monoliths and reactants. Conversely, reduced penetration depth of UV light into the reaction medium was probably responsible for the lower fuel production rate in the slurry system. Improved activity could also be due to the presence of the crystalline phase of anatase with a small percentage of rutile. The synergistic effect between the two crystalline phases probably retarded electron hole recombination through the creation of energy wells which serve as an electron trap formed from the lower band gap of rutile [36]. The extent of mixing and mass transfer rate have been identified as the essential difference between the slurry batch and the continuous gas phase monolith reactors in the degradation of 1,2-dichlorobenzene in waste water stream [37]. Comparison between these systems has identified the difficulty in maintaining homogeneous dispersion due to particles aggregation and insufficient light utilization by titania particles as drawbacks in slurry reactor compared to continuous gas phase monolith systems. They also observed that the latter presented better processing rates and throughput compared to the former, i.e. the slurry batch reactor is limited in the processing volume of the reactants at any given time as opposed to larger reactant volume in the continuous gas phase monolith systems.

Due to the different configurations of the photoreactors, the estimation of the space yield or throughput, product rate and quantum efficiency were used as standards for evaluating the performance of CO<sub>2</sub> photoreduction in our system. Table 5 highlights the optimal parameters used in both systems for these quantifications. The space yield which represents the production rate formed per time and volume of the reactor was higher in the internally illuminated

**Table 5**

Comparison between the slurry and internally illuminated monolith photoreactor using the 1 wt% Pd/0.01 wt% Rh-TiO<sub>2</sub> catalyst.

System	Slurry batch annular reactor	Internally illuminated monolith reactor
Catalyst loading <sup>a</sup>	0.1522 g	0.1099 g
Light source	Mercury lamp, UVA 41.62 mW/cm <sup>2</sup>	Mercury lamp, UVA 3.22 mW/cm <sup>2</sup>
Pressure	1.0 bar	1.0 bar
Temperature	25 °C	25 °C
Product type	Methane	Methanol/Acetaldehyde
Product rate (μmol/g-cat h)	0.03	0.10/0.21 <sup>b</sup>
Space yield (μmol/h m <sup>3</sup> ) <sup>c</sup>	42.28	50.88/106.85
Quantum efficiency <sup>d</sup>	0.002%	0.015%/0.047%

<sup>a</sup> Catalyst loading was measured from the difference between the dry weight of the monoliths coated with SiO<sub>2</sub> and M-TiO<sub>2</sub> where M represents the metal.

<sup>b</sup> Production rate was derived from the average production rate following 4 h of light irradiation.

<sup>c</sup> Space yield was measured based on the reactor volume of 216 cm<sup>3</sup>.

<sup>d</sup> Quantum efficiency = (number of electrons (n) × mole of hydrocarbon production rate/mole of UV photon absorbed by the catalyst) × 100 where n represents 6 for methanol, 8 for methane and 12 for acetaldehyde.

monolith reactor than the slurry batch reactor. The product rate of the 1 wt% Pd/0.01 wt% Rh-TiO<sub>2</sub> catalyst is higher in the internally illuminated monolith reactor than the slurry batch annular reactor (Table 5). The photon flow for each reactor system must also be considered when calculating the quantum efficiency which represents the number of reacted molecules per photon absorbed [23]. The quantum efficiency of the internally illuminated monolith reactor, 0.047% is 23.5 times higher than that of the slurry batch annular reactor, 0.002%. This is due to the low light utilization efficiency of the slurry reactor which results from absorption and scattering of the light by the reaction medium. There is also restricted processing capacity due to mass transport limitations [21]. Conversely, higher conversion efficiency has been demonstrated with the monolith photoreactor due to its flexible configuration, which allows maximum exploitation of the combined advantages of the high surface area of the monolith and the elimination of uneven light distribution via the optical fibres.

#### 4. Conclusions

The presence of Pd and Rh were found to improve the functional properties and photocatalytic activity of TiO<sub>2</sub> for CO<sub>2</sub> photoreduction under UVA light irradiation. By varying the configuration of catalyst particles in different photoreaction systems, we were able to demonstrate that better fuel production rates can be obtained by simultaneously using efficient supports and metal co-doping. Improved activity was observed over metal loaded TiO<sub>2</sub> ceramic honeycomb monolithic structures threaded with optical fibres than the metal loaded TiO<sub>2</sub> nanoparticles suspended in aqueous media. This could be due to increased contact efficiency between the monoliths and reactants which increased active sites and eliminated limited light penetration through the internal channels. The quantum efficiency of the internally illuminated monolith reactor was 23.5 times higher than that of the slurry batch annular reactor due to the combined advantages of the high surface area of the monolith and the elimination of uneven light distribution via the optical fibres being exploited.

#### Acknowledgements

The authors thank the financial support provided by the University of Nottingham and the Centre for Innovation in Carbon Capture and Storage (EPRSC grant EP/F012098/1). This work was also supported by the Royal Society International Project (JP090075), and Taiwan Collaboration Project (NSC 99-2911-I-002-106). M. Maroto-Valer is grateful for the support from the Leverhulme Trust (Philip Leverhulme Prize).

#### References

- [1] T.-V. Nguyen, J.C.S. Wu, Solar Energy Materials and Solar Cells 92 (2008) 864–872.
- [2] O. Carp, C.L. Huisman, A. Reller, Progress in Solid State Chemistry 32 (2004) 33–177.
- [3] H. Slamet, E. Purnama, S. Kosela, J. Gunlazuardi, Chemical Communications 6 (2005) 313–319.
- [4] D. Liu, Y. Fernández, O. Ola, S. Mackintosh, M. Maroto-Valer, C. Parlett, A. Lee, J. Wu, Catalysis Communications 25 (2012) 78–82.
- [5] O. Ishitani, C. Inoue, Y. Suzuki, T. Ibusuki, Journal of Photochemistry and Photobiology A 72 (1993) 269–271.
- [6] F. Solymosi, I. Tombacz, Catalysis Letters 27 (1994) 61–65.
- [7] M. Sahu, P. Biswas, Nanoscale Research Letters 6 (2011) 441–454.
- [8] P. Usubharatana, D. McMartin, A. Veawab, P. Tontiwachwuthikul, Industrial and Engineering Chemistry Research 45 (2006) 2558–2568.
- [9] M. Bideau, B. Claudel, C. Dubien, L. Faure, H. Kazouan, Journal of Photochemistry and Photobiology A 91 (1995) 137–144.
- [10] A.K. Ray, A. Beenackers, Catalysis Today 40 (1998) 73–83.
- [11] A.K. Ray, Chemical Engineering Science 54 (1999) 3113–3125.
- [12] P.S. Mukherjee, A.K. Ray, Chemical Engineering and Technology 142 (1999) 253–260.
- [13] M.F.J. Dijkstra, H. Buwalda, A.W.F. de Jong, A. Michorius, J.G.M. Winkelmann, A.A.C. Beenackers, Chemical Engineering Science 56 (2001) 547–555.
- [14] Y.-H. Yu, Y.-T. Pan, Y.-T. Wu, J. Lasek, J.C.S. Wu, Catalysis Today 174 (2011) 141–147.
- [15] N.J. Peill, M.R. Hoffmann, Environmental Science and Technology 29 (1995) 2974–2981.
- [16] B. Sanchez, A.I. Cardona, M. Romero, P. Avila, A. Bahamonde, Catalysis Today 54 (1999) 369–377.
- [17] R.-D. Sun, A. Nakajima, I. Watanabe, T. Watanabe, K.J. Hashimoto, Journal of Photochemistry and Photobiology A 136 (2000) 111–116.
- [18] J.T. Carneiro, R. Berger, J.A. Moulijn, G. Mul, Catalysis Today 147 (2009) S324–S329.
- [19] J. Xu, Y. Ao, D. Fu, J. Lin, Y. Lin, X. Shen, C. Yuan, Z. Yin, Journal of Photochemistry and Photobiology A 199 (2008) 165–169.
- [20] W. Wang, Y. Ku, Chemosphere 50 (2003) 999–1006.
- [21] T.-V. Nguyen, J.C.S. Wu, Applied Catalysis A – General 335 (2008) 112–120.
- [22] H. Lin, K. Valsaraj, Journal of Applied Electrochemistry 35 (2005) 699–708.
- [23] P. Du, J. Carneiro, J.T. Moulijn, G. Mul, Applied Catalysis A – General 334 (2008) 119–128.
- [24] P. Liou, S. Chen, J.C. Wu, D. Liu, S. Mackintosh, M. Maroto-Valer, R. Linforth, Energy & Environmental Science 4 (2011) 1487–1494.
- [25] J.C.S. Wu, I.-H. Tseng, W.-C. Chang, Journal of Nanoparticle Research 3 (2001) 113–118.
- [26] L.H. Ahrens, Geochimica et Cosmochimica Acta 2 (1952) 155–169.
- [27] C.D. Wagner, A.V. Naumkin, A. Kraut-Vass, J.W. Allison, C.J. Powell, J.R. Rumble, NIST X-ray Photoelectron Spectroscopy Database, vol. 20, 2007, Version 3.5.
- [28] K. Noack, H. Zbinden, Catalysis Letters 4 (1990) 145–146.
- [29] I.-H. Tseng, W.-C. Chang, J.C.S. Wu, Applied Catalysis B: Environmental 37 (2002) 37–48.
- [30] O. Ishitani, C. Inoue, Y. Suzuki, T. Ibusuki, Journal of Photochemistry and Photobiology A: Chemistry 72 (1993) 269–271.
- [31] T. Yui, A. Kan, C. Saitoh, K. Koike, T. Ibusuki, O. Ishitani, ACS Applied Materials & Interfaces 3 (2011) 2594–2600.
- [32] F. Solymosi, I. Tombacz, J. Koszta, Journal of Catalysis 95 (1985) 578–586.
- [33] A. Erdohelyi, M. Pasztor, F. Solymosi, Journal of Catalysis 98 (1986) 166–177.
- [34] F. Solymosi, A. Erdohelyi, M. Lancz, Journal of Catalysis 95 (1985) 567–577.
- [35] J.A. Dean (Ed.), Lange's Handbook of Chemistry, McGraw-Hill, United States, 1999, p. 4.80.
- [36] P. Bouras, E. Stathatos, P. Lianos, Applied Catalysis B: Environmental 73 (2007) 51–59.
- [37] H.F. Lin, R. Ravikrishna, K.T. Valsaraj, Separation and Purification Technology 28 (2002) 87–102.